Temperature field regulation of a droplet by

acoustothermal heater

Movies

Movie S1: Deformation of the 4-μL water-glycerol droplet in the process of first excitation. Captured at 100 frames/s.

Movie S2: In the subsequent heating process, the diameter of 4-μL water-glycerol droplet maintains constant. Surface vibration with an amplitude of 40 μm is observed at 100 frames/s.

Movie S3: Another vibration mode with higher frequency but smaller amplitude exists in the 4-μL water-glycerol droplet during the heating process. Captured at 6000 frames/s.

Movie S4: For the 4-μL pure glycerol droplet, surface vibration is hardly observed in the heating process. Captured at 100 frames/s.

A 24.6MHz

B 24.6MHz

SAW → Substrate (nm)

40μm
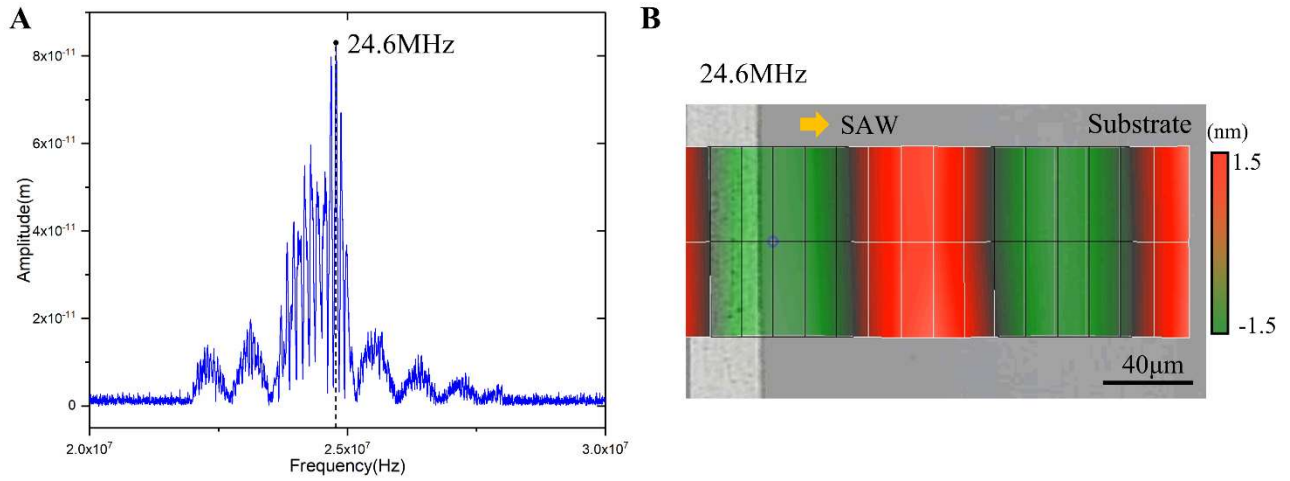
Figure. S1. (A) Amplitude spectrum of the vertical vibration on the LN substrate near the location of droplet. The maximum amplitude corresponds to the excitation frequency 24.6 MHz. (B) Amplitude of the vertical vibration corresponding to 24.6 MHz in a small region. The small region (80 μm × 320 μm) of the substrate, which locates between the IDTs and the droplet, is selected and scanned by 51 points.

Finite element analysis: The heating process of various droplets on the LN substrate was analyzed by a multi-physics-based finite element method in COMSOL Multiphysics 5.4. The microfluidic heater is modeled by a 500-μm piezoelectric substrate Ω_S with IDTs, an undeformed droplet Ω_D with contact angle 50°, and the adjacent air domain Ω_A (Fig. S2). 30 pairs of IDTs with a spatial period of 160 μm are treated as massless conductors due to their small thickness (200 nm). An electric potential with 5 V is imposed on the IDTs to make the vibration amplitude of the LN surface correspond to the measurement. The adopted material parameters are listed in the *Material Parameters section*, and the ambient temperature is set to 21 °C. Nonisothermal flow, the coupling of heat transfer and laminar flow are considered in the Ω_A, whereas only the heat transfer process in Ω_S and Ω_D is considered. We apply slip and non-slip boundary to air-droplet interface ($\mathcal{L}_D$) and air-substrate interface ($\mathcal{L}_S$), respectively. In addition, a boundary describing the connection with a larger volume of air, $(-p + 1/3 \cdot \mu \nabla \boldsymbol{u})\boldsymbol{n} = 0, \boldsymbol{t} \cdot \boldsymbol{u} = 0$ (where $\boldsymbol{n}$ and $\boldsymbol{t}$ are normal and tangential unit vector, p and $\boldsymbol{u}$ are pressure and velocity of the air domain, respectively), is applied to the outer surface ($\mathcal{L}_A$) of the air domain. With pre-derived heat source in Ω_S and Ω_D, transient temperature field is solved in the time domain.
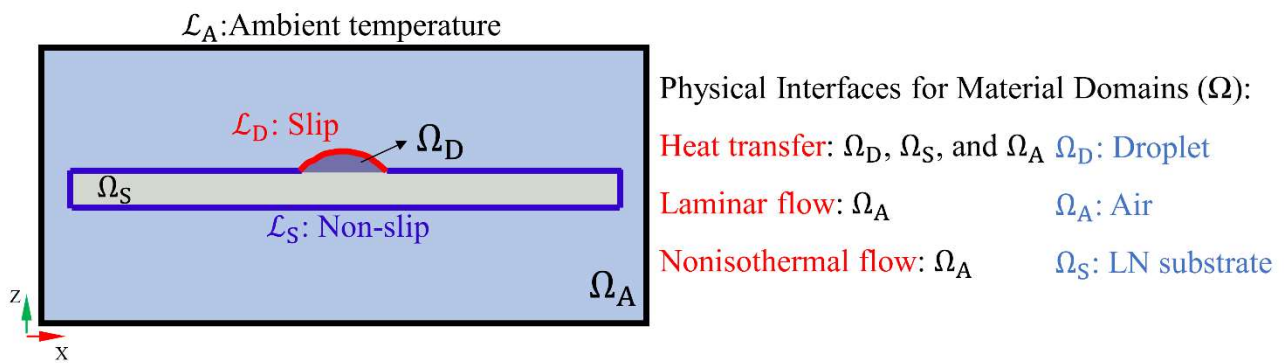
Figure. S2. Multi-physics model of the acoustothermal heater used in finite element analysis. The model consists of the air (Ω_A), the LN substrate (Ω_S), and the droplet (Ω_D) domains. Nonisothermal flow, the coupling of heat transfer and laminar flow are considered in the Ω_A, whereas only the heat transfer equation is solved in Ω_S and Ω_D. The slip and non-slip boundary conditions are used for the air-droplet ($\mathcal{L}_D$) and air-substrate ($\mathcal{L}_S$) interfaces, respectively, while the outer surface ($\mathcal{L}_A$) of Ω_A is in contact with a larger volume of air.

When analyzing the effects of electric dissipation on the heating process, the geometry of our numerical model corresponds to the actual device (Fig. S3A). The electric field of the LN substrate

and current density on IDTs are solved at 24.6-MHz. Thus, the heat source density resulting from the dielectric loss is derived by $q_\mathrm{d} = 0.5\boldsymbol{D} \cdot \boldsymbol{E}tan\delta(f)$, where $\boldsymbol{E}$ is the electric field, $\boldsymbol{D}$ is the electric displacement, and $tan\delta(f)$ represents the frequency-dependent dielectric loss coefficient. The heat source density resulting from the Joule heat of IDTs can be also estimated by $q_\mathrm{J} = \boldsymbol{J}^2\sigma^{-1}$, where $\boldsymbol{J}$ is the current density, and σ is the conductivity of IDTs.
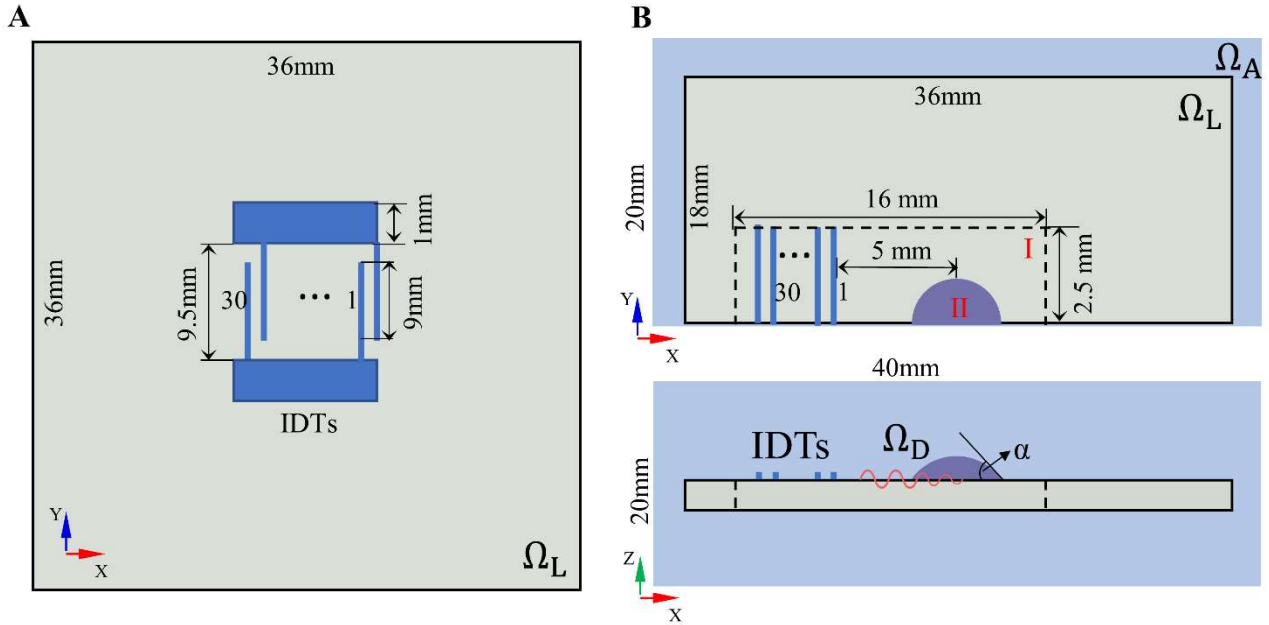

Figure. S3. **Geometry of the model**. (A) Geometry of the model corresponds to the actual device when analyzing the effects of the electric heat source. (B) A symmetric model for analyzing the effects of the acoustic heat source. For computational efficiency, a smaller substrate region (the regions I and II) only covering the center part of IDTs is used to derive the heat source density of the droplet. The heat transfer problems are still solved in the entire model.

For the effects of acoustic heat source, the electrical–mechanical and acoustic-structure coupling are taken into account. Considering the huge hard-source requirement in solving the 3-D acoustic-structure coupling problem, a symmetric model, only taking the center part of IDTs, is used to derive the heat source density (the regions I and II in Fig. S3B). Low-reflection boundary condition on the peripheries of LN substrate is used to suppress the reflected waves, while sound soft boundary is applied to the droplet surface. After solving the linear Helmholtz equation in the fluid domain, the acoustic heating source resulting from the viscous dissipation of leaky wave is calculated by Eq.1. Then the heat transfer problems are still solved in the entire model with geometric parameters corresponding to the actual device.

The effects of fluid motion due to the acoustic wave in the droplet are investigated by introducing an initial velocity field to the heat transfer process.[1] According to the perturbation theory of acoustic streaming, steady streaming in the droplet bulk is derived by solving the time-averaged second order Navier–Stokes equation,[2]

$$-\nabla \left\langle p_2 \right\rangle + \mu \nabla^2 \left\langle \boldsymbol{u_2} \right\rangle + (\mu_b + \frac{1}{3}\mu)\nabla(\nabla \cdot \left\langle \boldsymbol{u_2} \right\rangle) = \left\langle \rho_1 \partial_t \boldsymbol{u_1} \right\rangle + \rho_0 \left\langle (\boldsymbol{u_1} \cdot \nabla)\boldsymbol{u_1} \right\rangle \tag{S1}$$

where $\boldsymbol{u}$, p, and ρ are the velocity, pressure, and density of the fluid. The time-average operation $\langle X \rangle$ is given by $\langle X \rangle \equiv 1/t \int_0^t X(t)dt$ over a full oscillation period t. An additional term $\rho_0\langle(\boldsymbol{u_1} \cdot \nabla)\boldsymbol{u_1}\rangle$, the products of pre-derived first-order fields, acts as a body force in the governing equation, and generates the non-zero, time-averaged velocity field of the droplet in second order.
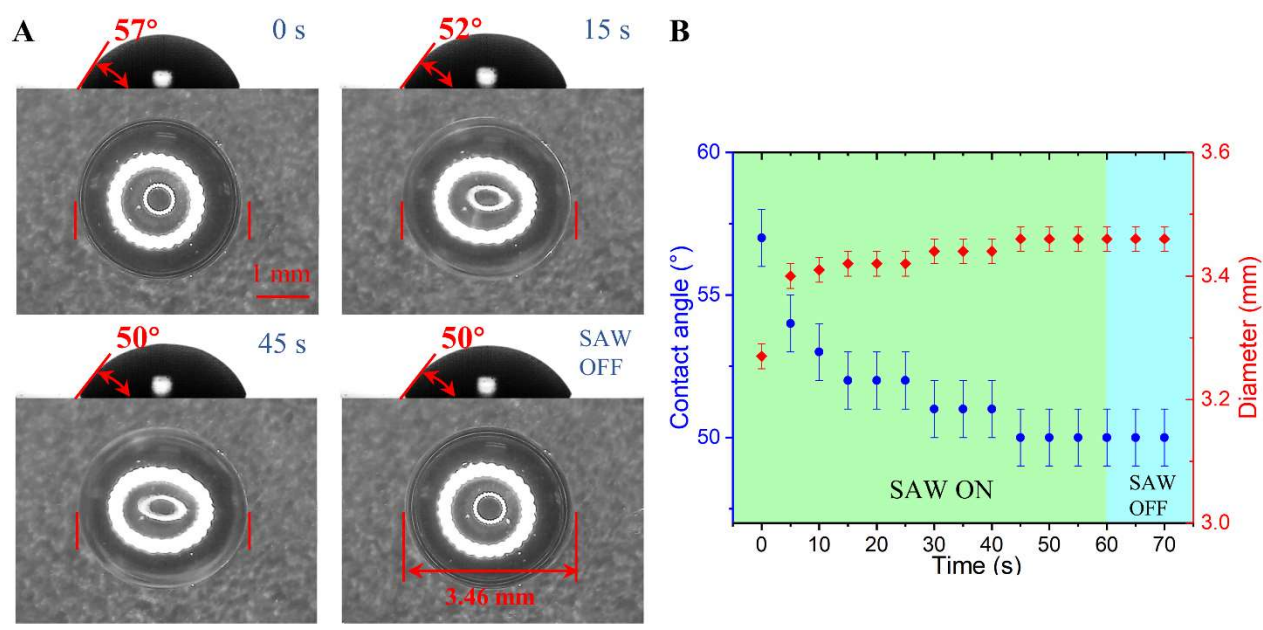
Figure S4. Static deformation of a 4 μL water-glycerol droplet in the process of first excitation. (A) After excitation, the contact angle of the droplet changes from 57° to 52° within 15 s, and then varies slightly (smaller than 2°). (B) Along with the decrease of contact angle, the droplet diameter increases, which gives a nearly constant volume in the heating process.
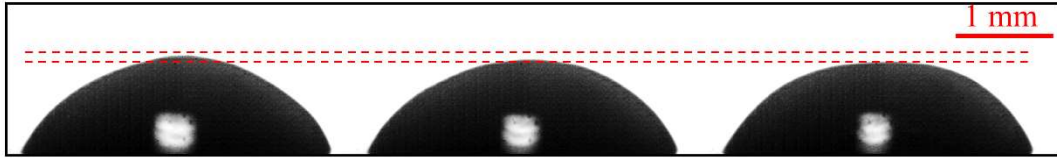
Figure. S5. Surface vibration of a 4 μL water-glycerol droplet during the heating process. The amplitude of surface vibration in the steady state is 40 μm.
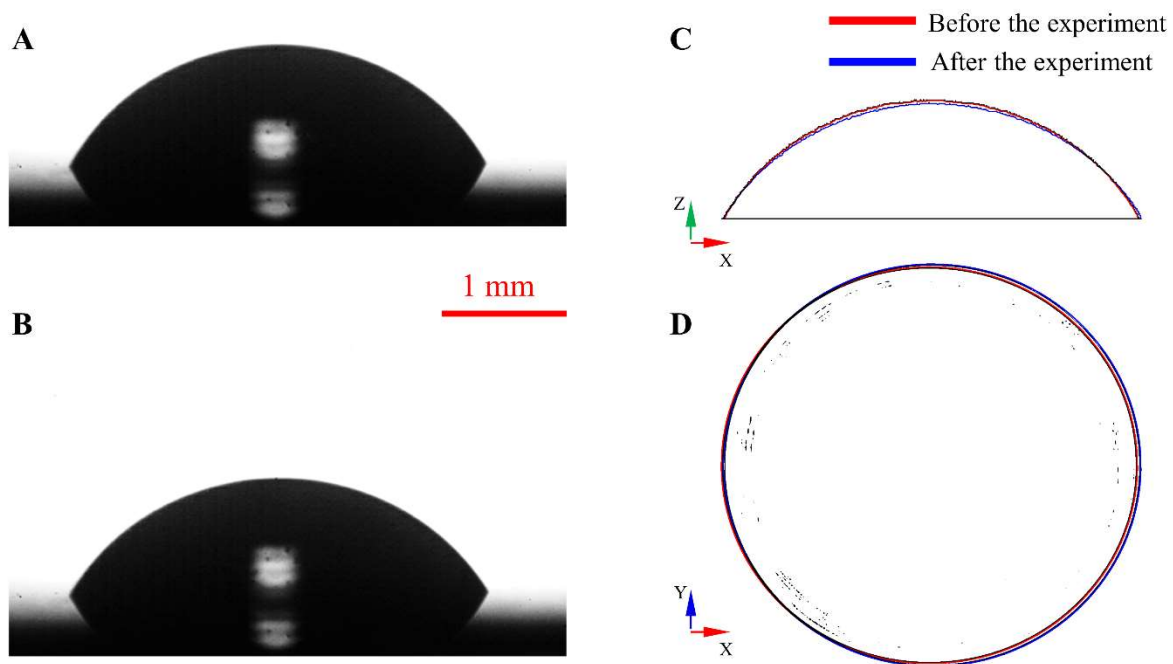
Fig. S6. (A) and (B) Images of the 4 µL water-glycerol droplet before and after the heating process. (C) and (D) Corresponding outlines of the droplet (red curve before excitation, blue curve after excitation), which is derived by using image processing.

$$Y_1 = 0.05x^2 + 19.5$$

$$Y_2 = 0.02x^2 + 20.46$$
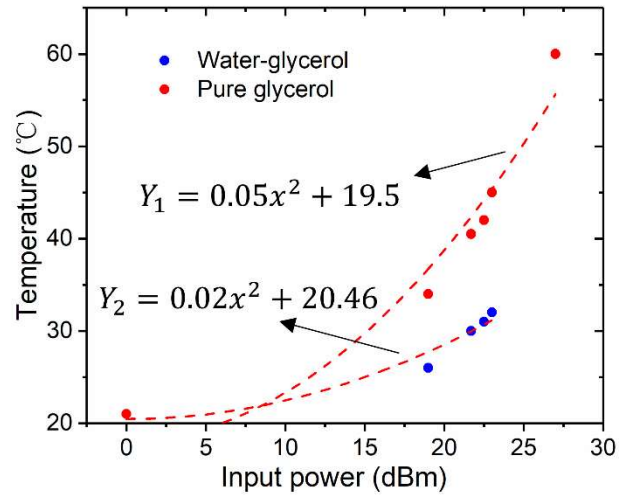
**Figure. S7**. Maximum temperature of a 4-μL water-glycerol and pure glycerol droplet as function of input electric power.

# Heating process of the droplet with the assumption of static inner fluid.
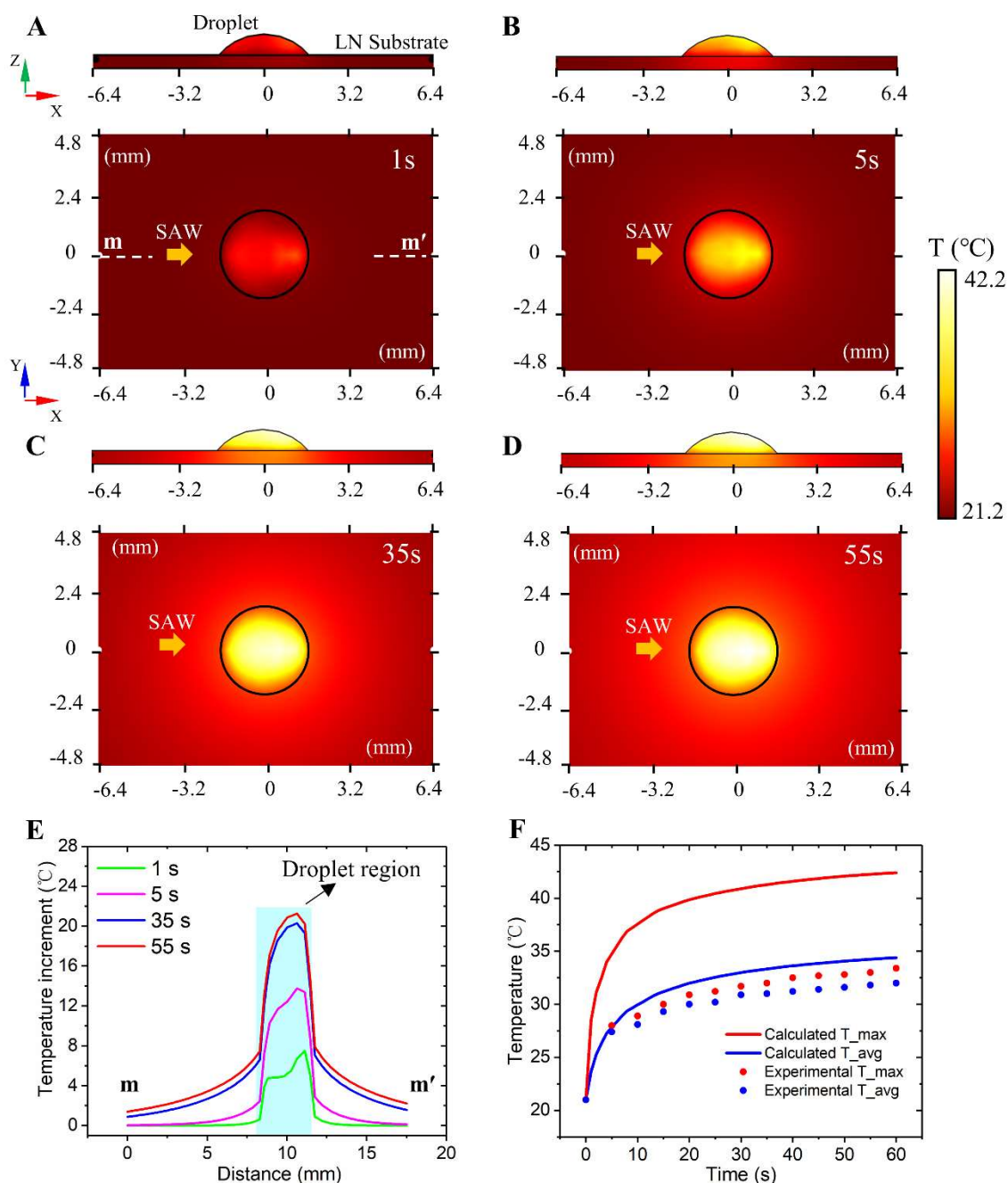
Figure S8. Predicted heating process of a 4 μL water-glycerol droplet with the assumption of static inner fluid. Temperature distribution on the x-z section and the upper surface of the device corresponding to different times (A) 1 s, (B) 5 s, (C) 35 s, and (D) 55 s. (E) Temperature increments along the centerline ("m-m'" in Fig. S4A). At the beginning (1 s), the region with the highest temperature appeared at the rear end. This region moves slightly forward in the heating process. Although the region with higher temperature remains at the right half of the droplet, the predicted equilibrium temperature field deviates from the experimental observation (Fig. 3E). (F) Predicted average and maximum temperature in the heating process overestimates the measurements.

Effect of thermal convection

Effects of thermal convection on the air-LN $\mathcal{L}_D$ and air-liquid $\mathcal{L}_D$ interfaces are analyzed by numerically solving the heat transfer equation (only in domain Ω_D and Ω_L) with amended boundary conditions (Fig. S9). Predicted heating processes of a 4 μL water-glycerol droplet show that thermal convection of the liquid-air surface plays a significant role in the heating process (Fig. S10). Although the liquid-air interface has a much smaller area compared to the air-LN interface, the induced acoustic streaming accelerates the heat flow on the air-LN interface.
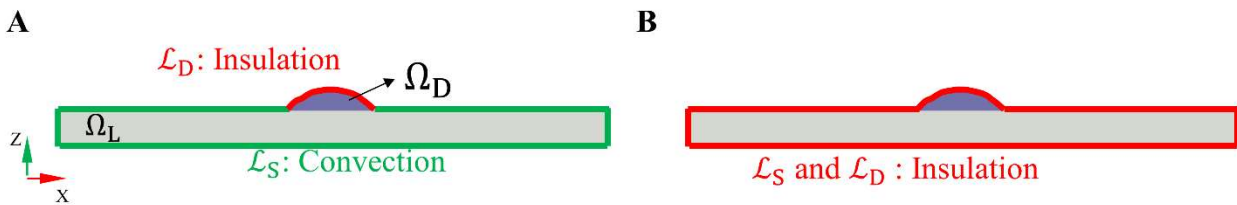

Figure S9. Boundary conditions used in the analysis of thermal convection effects. (A) Thermal insulation is applied on the droplet surface. (B) Thermal insulation is applied to the entire model.
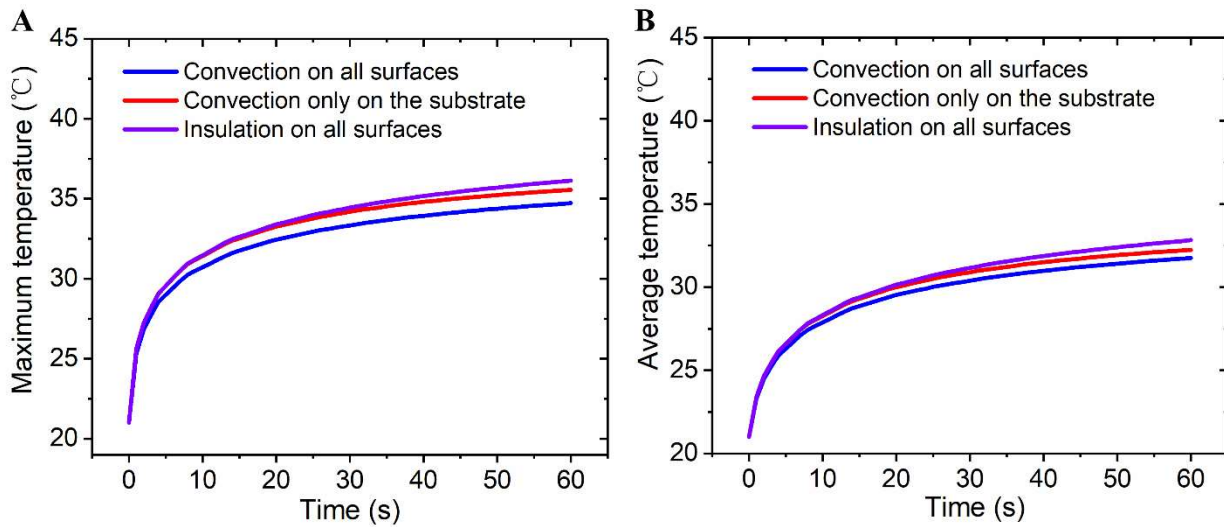
Figure S10. Effects of thermal convection on the heating process. Heating a 4 μL water-glycerol droplet is used as the modeling system. The maximum (A) and average temperature (B) are calculated with different thermal boundaries: convection on all surfaces (the result of Fig. S2), convection only on the substrate, and insulation on all the surfaces. Although the liquid-air interface has a much smaller area, its thermal convection effect plays a significant role in the heating process. The induced acoustic streaming also enhances the thermal convection of $\mathcal{L}_D$.

Effect of droplet-substrate size ratio
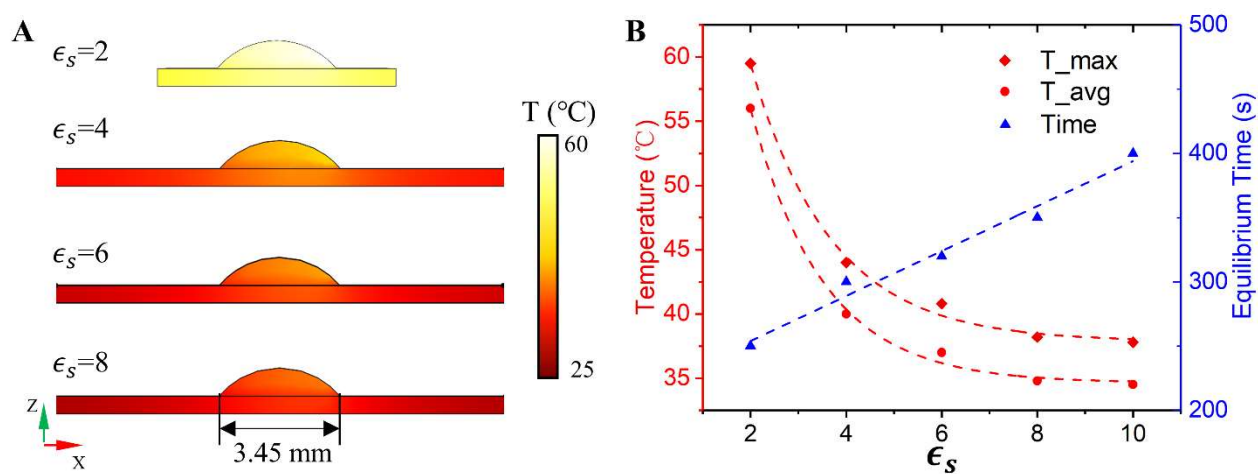
Figure S11. Effect of relative substrate size on the heating process. Also for a 4 μL water-glycerol droplet, the relative substrate size (ϵ_s=L/d) is defined as its edge lengths divided by the droplet contact diameter (d=3.45 mm). (A) Temperature distributions on the x-z plane for various ϵ_s, in which part of the substrate is demonstrated for $\epsilon_s = 4, 6, 8$. (B) Transition of the equilibrium temperature with the increase of ϵ_s. A larger ϵ_s needs more time to reach the equilibrium. When the ratio is larger than 8, the equilibrium temperature tends to be constant.
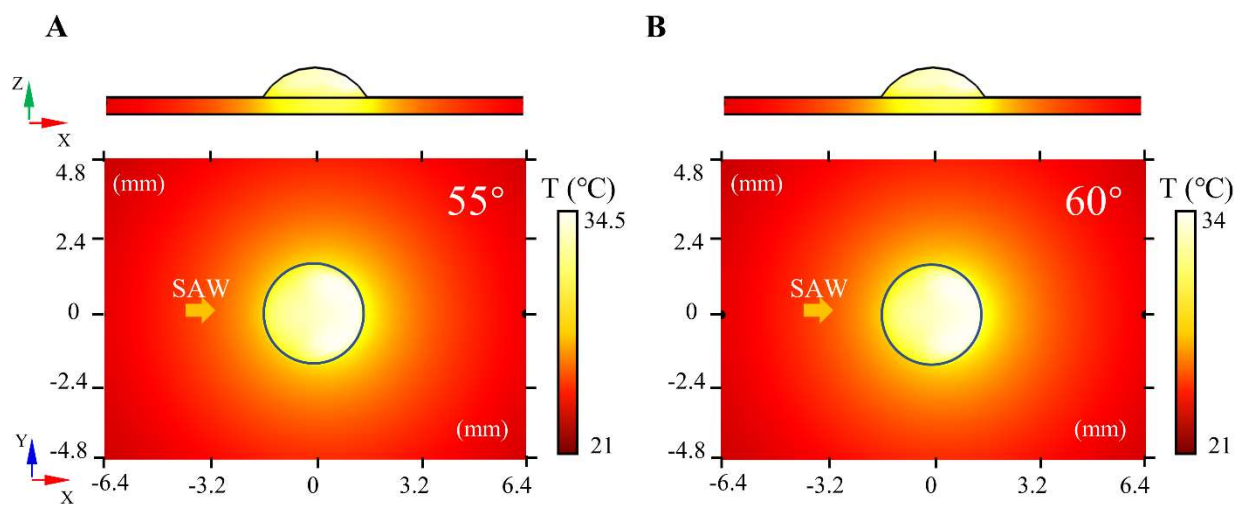
Figure S12. Predicted temperature distribution in a 4 µL water-glycerol droplet with (A) 55° and (B) 60° contact angle shows small differences.
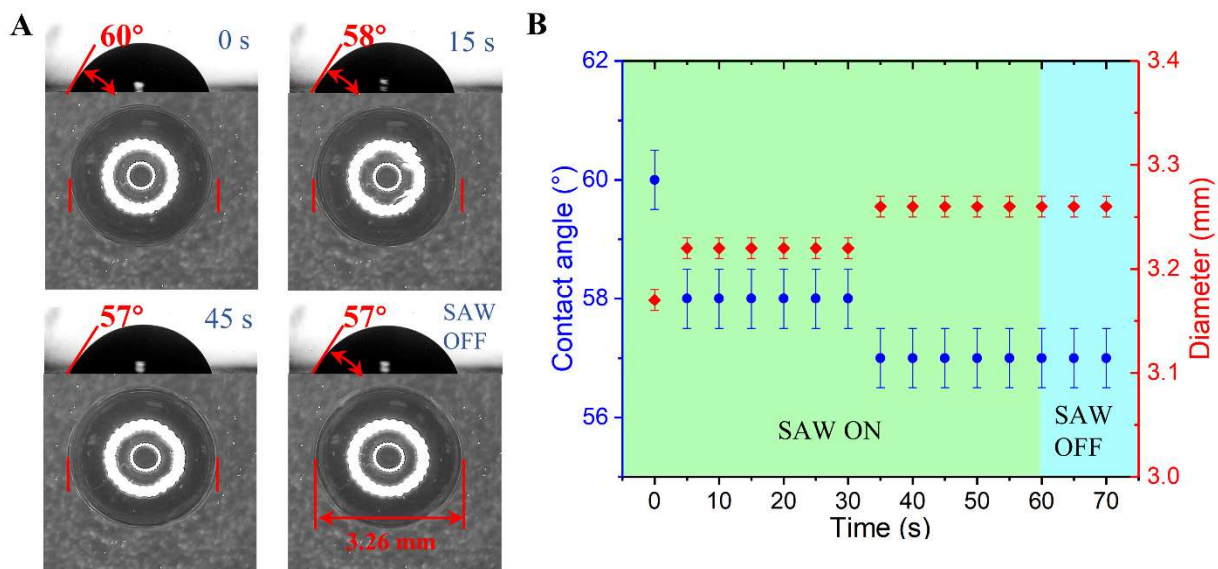
Figure. S13. Contact angle variation of a 4 µL glycerol droplet in the first excitation. (A) After exciting the device, the contact angle of the droplet changes from 60° to 58° within 15 s, and then varies slightly (smaller than 1°). (B) The droplet volume is almost constant during the heating process. In the subsequent excitations, the contact angle holds constant (Movie S4).

Distribution of the heat source

Table. S1. Distribution ratio of the heat source in various droplets.

	ϵ_f	Heat source (W)	Distribution ratio of the heat source	
			Front half	End half
Glycerol-water mixture	0.48	0.032	47%	53%
	0.77	0.052	45%	55%
	0.88	0.068	42%	58%
Glycerol	3.67	0.036	60%	40%
	5.80	0.066	75%	25%
	6.67	0.078	82%	18%

With the increase of ϵ_f, the end half of water-glycerol droplet possess more energy as heat source whereas heat source distributed in the front half of glycerol droplets has a larger ratio.

Material Parameters

The piezoelectric constant e_{kij}, dielectric constant ε_{ik}^S, and elastic stiffness constant c_{ijkl}^E of the LN substrate are [3]

$$[e] = \begin{bmatrix} 0 & 0 & 0 & 0 & 4.46 & 0.4 \\ -1.77 & 4.46 & -1.59 & 0.12 & 0 & 0 \\ 1.68 & -2.67 & 2.4 & 0.59 & 0 & 0 \end{bmatrix} \frac{\text{C}}{\text{m}^2}$$

$$[\varepsilon] = \begin{bmatrix} 44 & 0 & 0 \\ 0 & 37.9 & -7.81 \\ 0 & -7.81 & 34 \end{bmatrix} \frac{\text{F}}{\text{m}}$$

$$[c] = \begin{bmatrix} 20.3 & 7.23 & 6.02 & 1.07 & 0 & 0 \\ 7.23 & 19.4 & 9.06 & 0.89 & 0 & 0 \\ 6.02 & 9.06 & 22.03 & 0.81 & 0 & 0 \\ 1.07 & 0.89 & 0.81 & 7.49 & 0 & 0 \\ 0 & 0 & 0 & 0 & 5.63 & -0.44 \\ 0 & 0 & 0 & 0 & -0.44 & 7.6 \end{bmatrix} 10^{10} \frac{\text{M}}{\text{m}^2}$$

Table. S2. Material parameters used in the finite element analysis.

128° YX LiNbO₃ Substrate

Density	ρ_s	4700	kg/m^3
Speed of sound	c_s	3940	m/s
Thermal conductivity	k_s	4.18	$W/(m \cdot K)$
Specific heat capacity	C_s	628	$J/(kg \cdot K)$
Resistivity	ς	3×10^8	$\Omega \cdot cm$
Dielectric loss coefficient[4]	$tan\delta(f)$	0.16	1

Glycerol-water mixture (volume ration of 44%) [5]

Density	ρ_f	1210	kg/m^3
Speed of sound	c_f	1880	m/s
Shear viscosity	μ	25×10^{-3}	$Pa \cdot s$
Bulk viscosity	μ_b	42.4×10^{-3}	$Pa \cdot s$
Thermal conductivity	k_f	0.31	$W/(m \cdot K)$
Specific heat capacity	C_f	2500	$J/(kg \cdot K)$

Glycerol [5]

Density	ρ'_f	1260	kg/m^3
Speed of sound	c'_f	1930	m/s
Shear viscosity	μ'	300×10^{-3}	$Pa \cdot s$
Bulk viscosity	μ'_b	240×10^{-3}	$Pa \cdot s$
Thermal conductivity	k'_f	0.28	$W/(m \cdot K)$
Specific heat capacity	C'_f	2386	$J/(kg \cdot K)$

Aluminum IDTs

Density	ρ_{AL}	2700	kg/m^3
Thermal conductivity	k_{AL}	237	$W/(m \cdot K)$
Specific heat capacity	C_{AL}	904	$J/(kg \cdot K)$
Conductivity	σ	35.5×10^6	S/m

Reference

1. A. Riaud, M. Baudoin, O. Bou Matar, J.-L. Thomas and P. Brunet, 2016.

2. H. Bruus, *Lab Chip*, 2012, **12**, 20-28.

3. M. K. Tan, J. R. Friend, O. K. Matar and L. Y. Yeo, *Physics of Fluids*, 2010, **22**, 112112.

4. K. Nassau, H. J. Levinstein and G. M. Loiacono, *Journal of Physics and Chemistry of Solids*, 1966, **27**, 989-996.

5. A. Glycerine Producers, *Physical properties of glycerine and its solutions*, Glycerine Producers' Association, New York, 1963.